

## Comparing pseudopotential predictions for InAs/GaSb superlattices

G. C. Dente

*GCD Associates, Albuquerque, New Mexico 87110*

M. L. Tilton

*Boeing Defense and Space Group, Albuquerque, New Mexico 87106*

(Received 4 September 2001; revised manuscript received 30 July 2002; published 3 October 2002)

For several years, we have been accurately calculating the electronic structure of superlattices using a solution technique based on the empirical pseudopotential method. In our method for forming the superlattice pseudopotential, the critical assumption is that the heterointerface charges are redistributed, making each constituent layer in the superlattice as bulklike as possible. Here, we demonstrate that our technique for forming the superlattice pseudopotential is fundamentally different from the atomistic pseudopotential approaches that use a superposition of atomic pseudopotentials to represent the superlattice. We then present several applications of our method to InAs-GaSb type-II superlattices and, where possible, we compare our results to those calculated with an effective mass method, as well as to atomistic pseudopotential methods. In all of these comparisons, our method provides excellent agreement with the measured data.

DOI: 10.1103/PhysRevB.66.165307

PACS number(s): 71.55.Eq, 73.21.-b

### I. INTRODUCTION

Over the last decade, lasers, detectors, and other optoelectronic devices exploiting the unique electronic properties of heterostructures and superlattices have been developed. In many cases, these devices contain extremely thin layers composed of just a few atomic layers of semiconductor material. The widely used theoretical method for calculating the electronic and optical properties of these materials is based on  $\mathbf{k}\cdot\mathbf{p}$  perturbation theory and the envelope function approximation.<sup>1</sup> Indeed, this “effective mass” approach has been used so extensively that it has been referred to as the standard model.<sup>2</sup> Unfortunately, although the standard model has considerable intuitive appeal, the theoretical underpinnings for heterostructure applications remain controversial.

Pseudopotential techniques have often been suggested as more accurate alternatives to the standard model. The most commonly employed model forms the pseudopotential for the superlattice as a superposition of atomic pseudopotentials; we refer to this as the “atomistic” empirical pseudopotential method or AEPM. In contrast, our superlattice solution method, as originally presented in Ref. 3, requires an EPM description of the bulk component materials, and then, using only the energy-band lineups or offsets between component materials, fuses the bulklike layer potentials into the pseudopotential for the superlattice. This superlattice EPM, or SEPM offers several useful features.

(1) We form our pseudopotential for the superlattice by requiring that each layer remain as bulklike as possible. Once the compositional growth profile is specified, along with one offset parameter for each constituent pair, we construct the superlattice pseudopotential as described in Ref. 3.

(2) Rather than using a superlattice Bloch function that contains all plane waves represented by points from the origin out to a cutoff in the reciprocal lattice space of the superlattice, in many applications we can achieve excellent accuracy while using a much smaller set of plane waves represented by a cluster of superlattice reciprocal lattice

points centered on the bulk reciprocal lattice vectors.

(3) We can incorporate coherent strain effects in superlattice layers.

As in the standard model, the SEPM approach remains directly traceable to bulk constituents, while using a modest number of fit parameters for each constituent material. The critical SEPM assumption is that the heterointerface charges redistribute, forming charge and dipole sheets near the interface, in order that the layer pseudopotentials remain as bulklike as possible. This assumption, in turn, allows us to form the pseudopotential for the superlattice, while only introducing an offset parameter for each pair of materials in the superlattice. Furthermore, the construction only requires the bulk pseudopotential form factors for the constituent materials.

The first and second features prove to be very important, setting the SEPM apart from other atomistic pseudopotential treatments for superlattices.<sup>2,4</sup> Our method for forming the superlattice pseudopotential from the component material pseudopotential form factors is quite simple to implement, and, as we will further emphasize in Sec. II, it is fundamentally different from the AEPM methods employed by others. Furthermore, particularly for long-period superlattices, the approximation based on the smaller number of plane waves in the superlattice Bloch function can significantly lower the superlattice Hamiltonian matrix dimension. In many practical applications, this can lead to huge computational time reductions while sacrificing little, if any, accuracy. Indeed, over the last few years, all applications of our method have been successful, accurately predicting the measured subband energies in a wide variety of type-I and type-II superlattice samples.<sup>3,5-7</sup>

In the following sections, we will describe our approach for calculating the subbands of superlattices. Section II reviews our current understanding of the differences between our SEPM method and AEPM methods. Then, Sec. III presents several applications and comparisons to data. First, we calculate the band gap of InAs-GaSb superlattice samples, in

which the InAs and GaSb layer thicknesses are essentially equal. Next, we calculate band gaps and compare them to absorption data taken on several other InAs-GaSb superlattice samples. These samples show a strong blueshift for the band gap when the thickness of the InAs layer is held fixed, while the GaSb layer thickness is systematically increased.<sup>5,6</sup> For all of these applications, whenever possible, we compare our results to those calculated with an effective mass method, or standard model, as well as with AEPM methods. Section IV concludes the paper. The Appendix reviews an improved treatment for coherently strained superlattice materials.

## II. CHARGE REDISTRIBUTION AT THE SUPERLATTICE INTERFACES

The critical step in the SEPM occurs when we form the pseudopotential for the superlattice from the pseudopotentials that fit the bulk constituent materials. We assume that the heterointerface charges redistribute in order to make the pseudopotential in each material layer as bulklike as possible. For a two-component, lattice-matched superlattice, this leads to the SEPM approximation given as

$$V(\mathbf{r}) = \text{rect}\left(\frac{z}{w}\right) \sum_{\mathbf{g}} V_{\mathbf{g}}^W e^{i\mathbf{g}\cdot\mathbf{r}} + \left[1 - \text{rect}\left(\frac{z}{w}\right)\right] \sum_{\mathbf{g}} V_{\mathbf{g}}^B e^{i\mathbf{g}\cdot\mathbf{r}}, \quad (1)$$

in which the sums are over bulk reciprocal lattice vectors for the well and barrier materials.<sup>3</sup> Here, the sums represent the pseudopotentials for the infinitely extended bulk well and barrier materials using empirical form factors,  $V_{\mathbf{g}}^W$ ,  $V_{\mathbf{g}}^B$ , that reproduce the bulk band data for the well and barrier constituents. (Reference 16 gives an excellent review of the empirical pseudopotential method for fitting bulk band data.) We then use a finite Fourier series representation of the compositional profile functions to define the spatial variations for the well and barrier materials.<sup>3</sup> Once this Fourier series representation of the rect function is inserted, the pseudopotential of the superlattice is given as an expansion in the reciprocal lattice vectors of the superlattice. Note that the SEPM construction requires the same number of pseudopotential form factors used to fit the two bulk materials, as well as one additional parameter, essentially the difference of the  $\mathbf{g}=0$  form factors, to fix the offset between the materials; it is not likely that a smaller parameter set is possible. Equation (1) implies rapid variations of potential from a bulklike well layer to a bulklike barrier layer. Embedded in this SEPM approximation is the assumption that each layer retains its low-energy bulk configuration and that Eq. (1) approximates the self-consistent pseudopotential for the superlattice. Because the SEPM provides good agreement with the measured subband energies in a wide variety of type-I and type-II superlattice samples, we feel that the assumption of charge redistribution at the heterointerfaces is well supported. This approximation could break down for extremely thin layers, as, for example, those composed of one or two monolayers, but for the vast majority of superlattices used in practical devices, the SEPM approximation has proven to be exceptionally accurate.

This SEPM superlattice pseudopotential construction is quite different from those based on a superposition of atomic pseudopotentials. (See Refs. 2, 4, and 8, as well as the references cited therein.) In these AEPM approaches, one arrives at the pseudopotential for the superlattice by superimposing potentials for each ion site in the superlattice as

$$\bar{V}(\mathbf{r}) = \sum_{\beta} \sum_n \nu_{\beta}(\mathbf{r} - \mathbf{R}_n\beta), \quad (2)$$

in which  $\nu_{\beta}$  is the atomic pseudopotential for  $n$ th type- $\beta$  ion at location  $\mathbf{R}_n\beta$ . For InAs/GaSb superlattices, this construction requires, at the minimum, functional pseudopotential fits for “In in As,” “As in In,” “Ga in Sb,” and “Sb in Ga.” Then, to obtain an even more accurate description of the pseudopotentials near the heterointerfaces, one could consider additional functional pseudopotential fits for “In in Sb,” “Sb in In,” “Ga in As,” and “As in Ga.” Additionally, most of these bond types are highly strained, so that strain parameters are needed. Obviously, these AEPM approaches, for even a relatively simple two-component superlattice, can depend on a much larger number of adjustable parameters than the SEPM. We emphasize that these AEPM methods require accurate functional pseudopotential fits, not just a modest number of empirically adjusted form factors as used in SEPM. However, at first glance, the AEPM approach would appear sound and complete, allowing for microscopic detail such as the inclusion of interfacial segregation and intermixing.

When we compare Eq. (1) and Eq. (2) in detail, we find that Eq. (2) generates far gentler variations in potential at the heterointerfaces. We can illustrate these differences between Eqs. (1) and (2) by considering a one-dimensional superlattice created by the one-dimensional ionic pseudopotentials, shown in Fig. 1(a) for material A and material B. In Fig. 1(b), we show several periods of the atomistic superlattice pseudopotential for a superlattice with six A-lattice sites and twelve B-lattice sites per period of the superlattice. In comparison, Fig. 1(c) shows the superlattice pseudopotential resulting from the SEPM construction. The differences near the interfaces are significant, becoming even more pronounced with a longer range ionic potential. Ultimately, the accuracy of Eq. (1) or Eq. (2) for constructing the pseudopotential of the superlattice can only be determined by comparison to experiment.

## III. COMPARISON OF SOLUTIONS AND DATA FOR TYPE-II InAs/GaSb STRUCTURES

Some of the earliest superlattice research was based on the InAs/GaSb system.<sup>9</sup> In this section, we will apply the SEPM method to several InAs/GaSb samples. Whenever possible, we will make comparisons to predictions generated by the standard model and the AEPM methods.

First, we calculate the band edge of InAs-GaSb type-II superlattice samples, in which the thickness of the InAs and GaSb layers are essentially equal. As a first step in implementing SEPM, we need accurate EPM fits for both GaSb and strained InAs. The pseudopotential form factors listed in

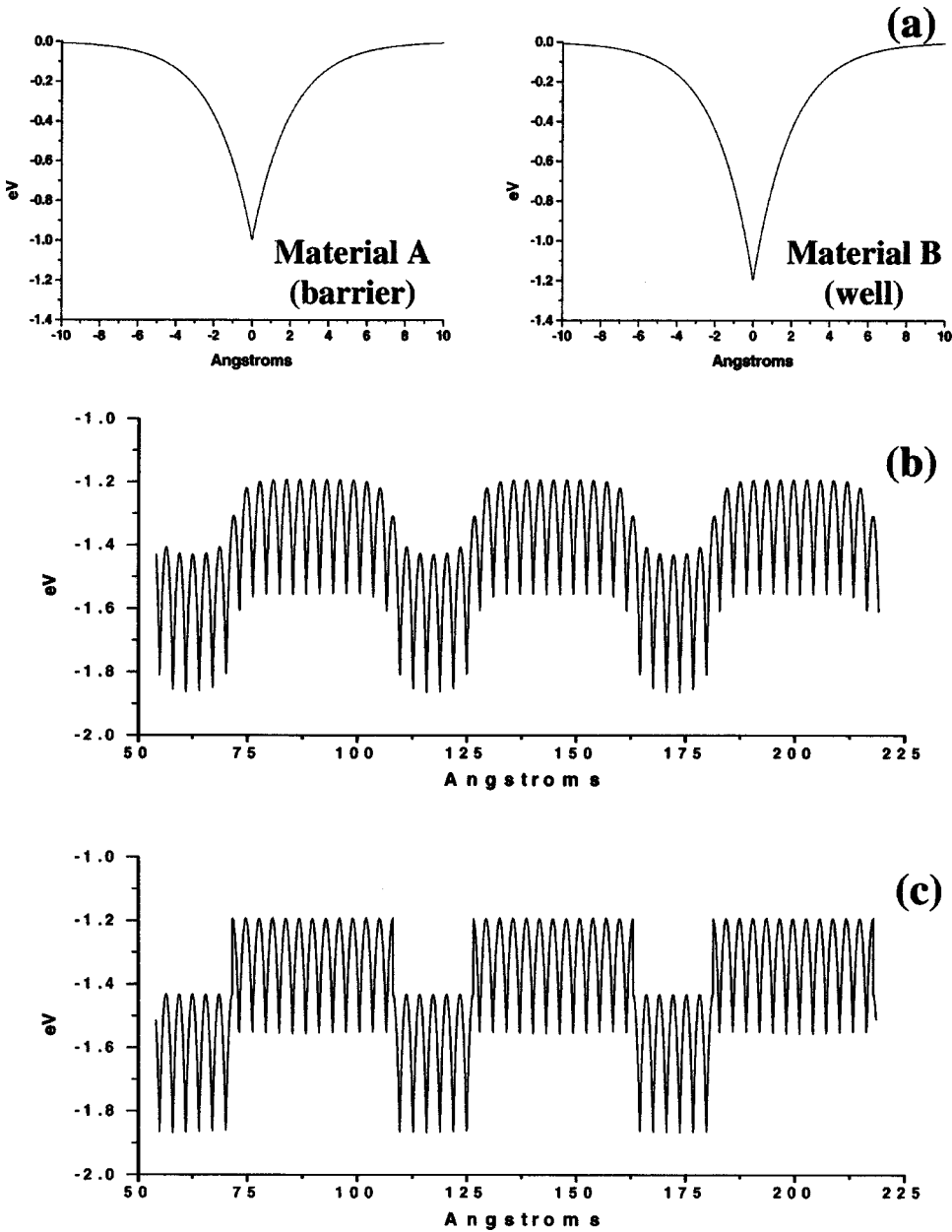


FIG. 1. Comparison of SEPM and atomistic EPM for one-dimensional case. (a) Ionic potentials for well material (A) and barrier material (B). (b) Atomistic EPM superlattice pseudopotential. (c) SEPM superlattice pseudopotential.

Table I were selected to fit the GaSb and InAs 77 K temperature data given in Ref. 10. Table II illustrates the resulting fit quality. The InAs is coherently strained to match the thick GaSb substrate (see the Appendix). In all of our calculations, once we fit the constituent materials, we make no further adjustments to the pseudopotential form factors for GaSb and InAs, we use the same form factors for all of the superlattice calculations. The EPM calculation for the InAs/GaSb superlattice requires a band offset input as well. We adjusted  $V_{g=0}^{\text{InAs}}$  so that the strained InAs conduction-band edge was 150 meV below the GaSb valence-band edge; this type-II offset value, which was fixed for all the samples, provides the best agreement with the data and is near the consensus value.<sup>8</sup> In Ref. 3, we introduced cutoffs in the Fourier series representation of the rect-function and the superlattice Bloch function; these cutoffs essentially limit the range of growth-direction-momentum values coupled by the superlattice. All

of the SEPM results were calculated with the cutoff  $M = 12$ ; when we doubled this cutoff to  $M = 24$  in the 12 ML/12 ML case, the band-edge energy changed by less than 0.0007 eV. Simultaneously, for all calculations, the cutoff in the superlattice Bloch function was fixed at  $N_F = M/2$ .

Figure 2 displays the calculated band-gap results for the InAs(N)/GaSb(N) samples versus layer thickness in angstrom. The experimentally determined band-gap results were extracted from several sources, as indicated in the figure. Unfortunately, it is impossible to assign error bars to the various data points, and, in addition, the reported values are usually photoluminescence peaks that should be at a slightly higher energy than the band edge. Along with this collage of data, we show band-edge predictions for the primary band gap from SEPM, two atomistic EPMs, and an eight-band  $\mathbf{k} \cdot \mathbf{p}$  theory.<sup>4,8</sup> Both the SEPM and the standard model predictions are in reasonable agreement with the data. However,

TABLE I. Pseudopotential form factors for InAs and GaSb at 77 K. (Note: InAs form factors represent InAs coherently strained to GaSb.)

	InAs	GaSb
$V_3^S$	-0.266	-0.249
$V_8^S$	0.018	0.050
$V_{11}^S$	0.047	0.032
$V_3^A$	0.070	0.038
$V_4^A$	0.038	0.004
$V_{11}^A$	0.010	0.035
$D_4^A$	0.460	
$\Gamma$	4100.0	13 800.0
$m/m_0$	0.9	0.9
$C_{11}$	8.329(6)	
$C_{12}$	4.526(6)	
$a_H$	-5.91	
$b$	-1.80	

TABLE II. SEPM band parameters for the bulk constituents, InAs and GaSb. The bulk InAs target values have been adjusted to bulk InAs coherently strained to GaSb. The lattice constant for both the strained InAs and GaSb is  $a = 6.0659 \text{ \AA}$ .  $\gamma_1$ ,  $\gamma_2$ , and  $\gamma_3$  are the Luttinger ( $\mathbf{k} \cdot \mathbf{p}$ ) parameters.  $E_g$  is the gap voltage,  $\Delta_0$  is the spin-orbit splitting,  $E_p$  is the  $s$ - $p$  mixing parameter, and  $m_{xx}$  are the effective masses in the directions specified.  $E_{VBO}$  is the valence-band offset between the InAs<sub>VBM</sub> and the GaSb<sub>VBM</sub>.  $a_c$  and  $a_v$  are the hydrostatic deformation potentials of the valence band and conduction band, respectively. We use the target values of these deformation potentials to calculate some of the strained InAs target values.  $X_{lc}$  and  $L_{lc}$  are the X and L conduction-band valley locations with respect to the valence-band edge at  $\Gamma=0$ . These values are calculated at the edge of the Brillouin zone.

	InAs (77 K)		GaSb (77 K)	
	SEPM fit	Target value	SEPM fit	Target value
$\gamma_1$	19.203	19.94	11.82	11.95
$\gamma_2$	8.665	8.5	4.31	4.10
$\gamma_3$	9.083	9.42	5.27	5.33
$E_g$ (eV)	0.368	0.371	0.8	0.8
$\Delta_0$ (eV)	0.380	0.390	0.682	0.75
$E_p$ (eV)	19.60	19.9	22.45	22.60
$\Delta E_{VBO}$ (eV)			0.540	0.540
$m_e$	0.0221	0.0220	0.043	0.0405
$m_{lh}$ [001]	0.0274	0.0271	0.053	0.0496
$m_{hh}$ [001]	0.534	0.340	0.313	0.267
$m_{hh}$ [111]	0.964	0.909	0.780	0.775
$m_{so}$ [001]	0.0982	0.0928	0.133	0.135
$a_c$		-4.91		-7.379
$a_v$		-1.0		-0.79
$X_{lc}$ (eV)	2.27	2.28	1.42	1.7
$L_{lc}$ (eV)	1.93	1.53	1.43	1.2

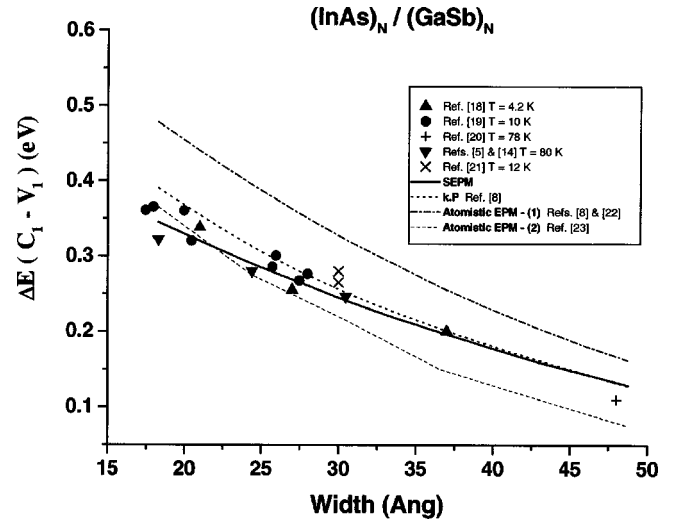


FIG. 2. Data on InAs( $n$  ML)/GaSb( $n$  ML) superlattices from several sources.<sup>5,8,18–23</sup> Calculated results for SEPM, atomistic 1, atomistic 2, and  $\mathbf{k} \cdot \mathbf{p}$ .

the SEPM results seem to be more accurate over the full range of thicknesses, since they are on the low-energy edge of the data. In comparison, the AEPM method of Ref. 8 appears to consistently overestimate band gaps in these InAs/GaSb superlattices with layer thicknesses less than 15 monolayers, while the AEPM results from Ref. 4 are only accurate over a very limited range of thicknesses.

Next, we address an interesting band-gap effect that was recently reported in Ref. 5. Two sets of InAs/GaSb type-II superlattice samples, with 30 periods each, were grown and characterized. In one set of five samples, the InAs layer thickness, per period, was fixed at 6 ML (monolayers), while the GaSb layer thickness was nominally 6, 9, 12, 18, and 24 ML per period. In the second set of six samples, the InAs layer thickness, per period, was 8 ML, while the GaSb layer thickness was nominally 8, 12, 16, 24, 32, and 40 ML. The samples showed a significant spectral blueshift with increasing GaSb thickness.<sup>5</sup> For example, the InAs(6 ML)/GaSb(6 ML) superlattice sample showed a  $3.8 \mu\text{m}$  absorption edge, while the InAs(6 ML)/GaSb(24 ML) sample showed a  $2.9 \mu\text{m}$  absorption edge, both at 80 K.

Figures 3(a) and 3(b) show our SEPM calculations for the band-edge wavelength for both the InAs 8 and 6 ML cases, along with the Fourier transform infrared determined absorbance edge for the samples. The absorbance data were taken at 77 K and were consistent with photoluminescence data.<sup>5</sup> The observed spectral shift of the absorbance edge with increasing GaSb thickness was significant in both samples. The SEPM method accurately predicts these observations. For comparison, again in Figs. 3(a) and 3(b), we show a complete set of band-edge predictions generated by an eight-band  $\mathbf{k} \cdot \mathbf{p}$  calculation.<sup>12</sup> On the same two figures, we have also plotted the available data generated by two different research groups that used an AEPM approach. The “atomistic EPM 1” results in Fig. 3(a) were assembled from Refs. 8 and 11. The four “atomistic EPM 2” results in Figs. 3(a) and 3(b) were extracted from Ref. 23. At this time, only the SEPM results are in good agreement with the data taken on

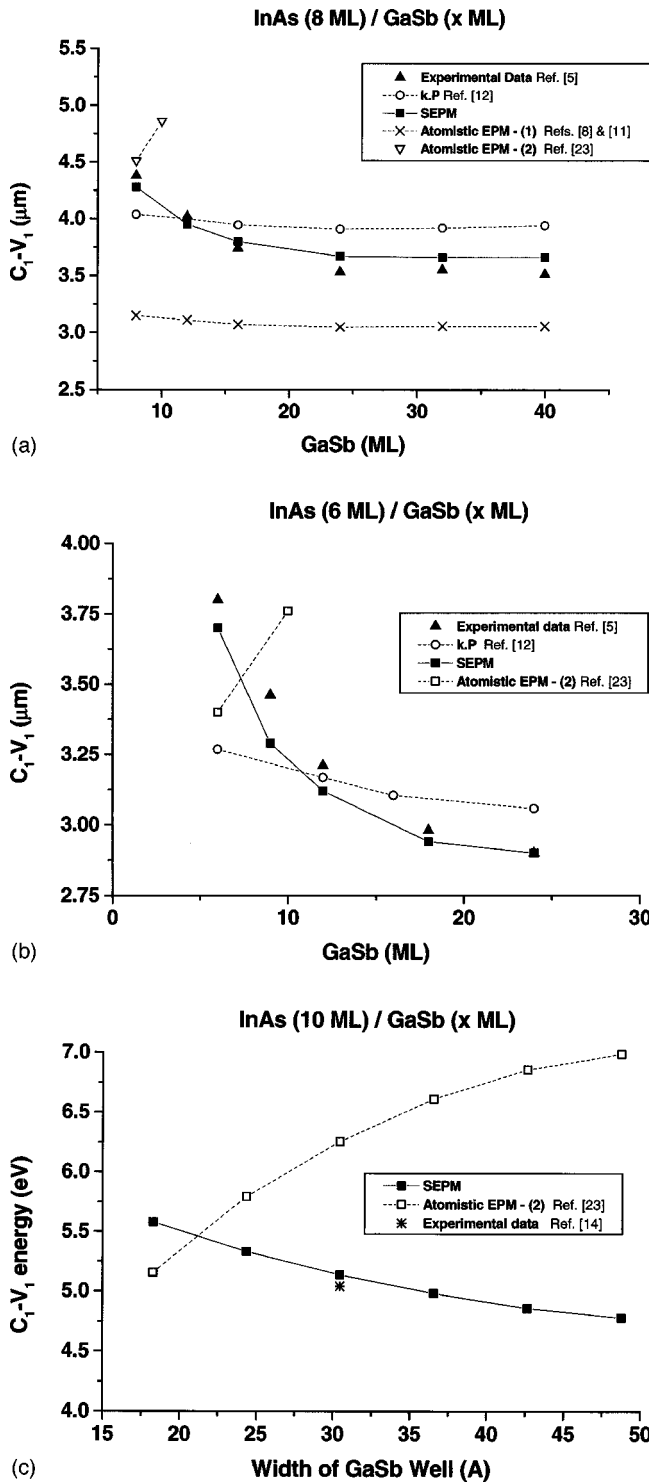


FIG. 3. Blueshift data from and calculated results. (a) InAs(8 ML)/GaSb( $\times$ ML) data and calculations. (b) InAs(6 ML)/GaSb( $\times$ ML) data and calculations. (c) InAs(10 ML)/GaSb( $\times$ ML) data and calculations.

the InAs 8 and 6 ML sample sets. (Some recent results suggest that the AEPM of Ref. 8 will generate significantly different results, in better agreement with the data, when interfacial segregation and intermixing are included, albeit at the expense of essentially doubling the fit parameters to allow

fitting the underlying binaries GaSb, InAs, GaAs, and InSb and their interfaces.<sup>13</sup> For example, one such modified calculation results in an  $\sim 157$  meV reduction in band-gap energy, for the InAs(8 ML)/GaSb(8 ML) superlattice with abrupt interfaces.)

Finally, in Fig. 3(c), we show the SEPM predictions and the “atomistic EPM 2” results from Ref. 23 for the case in which the InAs layer thickness per period was fixed at 10 ML and the GaSb thickness was increased. For this superlattice, the only experimental data point is at InAs(10 ML)/GaSb(10 ML).<sup>14</sup> Here, once again, the SEPM shows the blueshift trend while agreeing with the one measured point. The AEPM results from Ref. 23 are very inaccurate at the one data point, and furthermore, show a redshift that is contrary to the expected trend.

#### IV. CONCLUSIONS

We have demonstrated a direct generalization of the empirical pseudopotential method for application to both unstrained and strained superlattices. For a two-component superlattice, this superlattice EPM, or SEPM, uses a superlattice pseudopotential constructed from the bulk constituent pseudopotentials for the well and barrier materials as given by Eq. (1). This superlattice pseudopotential construction is fundamentally different from those based on a superposition of atomic pseudopotentials. This SEPM construction essentially fuses the infinitely extended bulk pseudopotentials for the components, imposing charge redistributions and large potential gradients at the interfaces between the well and barrier materials. These redistributions of heterointerface charges may be driven by the requirement that it is energetically preferable for the component layers to remain as bulk-like as possible. As an added practical benefit, the SEPM construction involves only a modest number of empirical pseudopotential form factors required to fit the two bulk materials, as well as an additional parameter to fix the offset between the materials. Certainly the most important observation, far outweighing any other features or concerns, is that this SEPM construction gives predictions that are in excellent agreement with a large database collected on a wide variety of type-I and type-II superlattices.

We then presented applications of the SEPM method to InAs/GaSb superlattices. First, we calculated the band edge of InAs/GaSb type-II superlattice samples in which the thicknesses of the InAs and GaSb layers were essentially equal. Next, we showed SEPM predictions for recent data showing a strong blueshift for the band edge of InAs-GaSb type-II superlattice samples, in which the thickness of the InAs layer was held fixed, while the GaSb layer thickness was systematically increased. For these samples, the SEPM band-edge calculations appear to be quite accurate. In contrast, whenever published or reported data were available, the predictions of the standard model as well as the AEPM methods, did not measure up to the accuracy provided by the SEPM calculations. In particular, we feel that the recent blueshift results on the 6 ML InAs sample set and the 8 ML InAs sample set represent data for which the predictions of both the standard model and the AEPM approaches are very

inaccurate. (A revised envelope function calculation incorporating interface terms provides much improved agreement to the blueshift data. Reference 15 gives the details for this recent modification of the standard model.)

In summary, the SEPM method appears to provide an excellent approximation for the pseudopotential in many practical superlattices of current interest.<sup>3,5-7</sup> Admittedly, most of these applications have involved superlattices in which the thinnest layer per period was no less than 6 ML thick. For these cases, the assumption of heterointerface charge redistribution with each layer maintaining bulklike properties appears justified by the data. Perhaps, with very short-period superlattices, in which layers are thinned to one or two monolayers, it is likely that better accuracy will result from an atomistic approach, in which the pseudopotential of the short-period superlattice is represented as a sum over ionic potentials. Ultimately, the most microscopically correct theory for superlattices, with thick or thin layers, will probably be based on an atomistic approach, as well as a fully self-consistent, many-body calculation that allows for self-consistent charge redistribution at the heterointerfaces of the superlattice. Alternatively, for the present time, the SEPM offers an easily implemented, yet highly accurate method for calculating the electronic structure of superlattices.

#### ACKNOWLEDGMENTS

We thank Dr. R. Kaspi and Giovanni Donati for supplying us the photoluminescence data. This research was funded by the Air Force Research Laboratory's Directed Energy Directorate under contract to GCD Associates (Contract No. F29601-99-R-0005).

#### APPENDIX: INCORPORATING COHERENT STRAIN

Here, we offer a modification of our original procedure for representing the effects of coherent strain.<sup>3</sup> Lattice-mismatched layers can be grown if the layers are sufficiently thin. The resulting strain changes both the dimensions and the symmetry of the material, thereby perturbing the band diagram. In particular, the conduction-to-valence band gap, as well as the degeneracy and curvatures of the light-hole and heavy-hole bands, are changed. In the original treatment given in Ref. 3, we mimicked the symmetry-breaking features of strain by distorting the basis vector connecting the cation and anion in a unit cell. Although this approach would accurately split the light- and heavy-hole bands, leading to accurate results for several strained-layer superlattices, we were never satisfied with the approximation. Here, we will describe a more realistic and accurate method for accommodating strain into the pseudopotential calculations for strained-layer superlattices.

Consider a coherently strained zinc blende layer grown in the  $z$  direction on a substrate with lattice constant  $a$ . The strained material will have primitive direct lattice vectors given by

$$\mathbf{d}_1 = \frac{a}{2}(0, 1, 1 + \mu), \quad \mathbf{d}_2 = \frac{a}{2}(1, 0, 1 + \mu), \quad \mathbf{d}_3 = \frac{a}{2}(1, 1, 0), \quad (\text{A1})$$

in which  $\mu = -2(C_{12}/C_{11})\varepsilon$  relates the lattice change in the growth direction to the percentage of strain,  $\varepsilon$ ; strain is negative for compressive-strained material and positive for tensile-strained material. Also,  $C_{11}$  and  $C_{12}$  are the elastic moduli. In addition, the strained basis separation vector connecting the cation to the anion is given by  $2\boldsymbol{\omega} = a/4(1, 1, 1 + \mu)$ . The first fifteen reciprocal lattice vectors for the strained lattice are then given as

$$\begin{aligned} \mathbf{h}_0 &= \frac{2\pi}{a}(0, 0, 0), \quad \mathbf{h}_{1,\dots,8} = \frac{2\pi}{a}[\pm 1, \pm 1, \pm 1/(1 + \mu)], \\ \mathbf{h}_{9,12} &= \frac{2\pi}{a}[0, 0, \pm 2/(1 + \mu)], \\ \mathbf{h}_{10,33} &= \frac{2\pi}{a}(0, \pm 2, 0), \quad \mathbf{h}_{11,14} = \frac{2\pi}{a}(\pm 2, 0, 0), \end{aligned} \quad (\text{A2})$$

so that the  $z$  component of every reciprocal lattice vector is multiplied by the same factor.

Our calculations for strained-layer superlattices are tremendously simplified if we do not break the lattice symmetry, but instead, only break the symmetry of the potential at each lattice site. In this approximation, we break the symmetry of the empirical form factors; next, we directly apply the lattice-matched superlattice EPM method described in the Ref. 3 to strained-layer superlattices. We accomplish this by empirically adjusting the magnitude-three (mag-3) and mag-4 form factors in the perturbed matrix elements. In following, we use  $\Omega_g$  to label the pseudopotential form factors for the strained material.

For the mag-3 reciprocal lattice vectors, indexed 1, 2, ..., 8, the magnitudes of the strained reciprocal lattice vectors are equal for the set and given by

$$(h)^2 = (2\pi/a)^2[2 + (1 + \mu)^{-2}]. \quad (\text{A3})$$

Therefore, the form factors for mag-3 are all changed by the same amount, and the hydrostatic component of strain can be incorporated by making slight pseudopotential form factor adjustments in  $\Omega_3^S$ ,  $\Omega_3^A$  to match the measured hydrostatic, strain-induced modification of the conduction to valence band gap. This band-gap change is often calculated as

$$\Delta E = (-a_H)2 \frac{C_{11} - C_{12}}{C_{11}} \varepsilon, \quad (\text{A4})$$

in which  $a_H$  is the hydrostatic deformation potential. The band gap increases for a compressive strain and decreases for a tensile strain.<sup>17</sup>

For the reciprocal lattice vectors 9 and 12, the magnitude of the strained reciprocal lattice vectors is given by

$$(h)^2 = (2\pi/a)^2 4(1 + \mu)^{-2} \rightarrow \Omega_4^A \approx V_4^A + D_4^A(h - g), \quad (\text{A5})$$

so that the antisymmetric pseudopotential form factor is slightly perturbed for vectors 9 and 12 by an expression linear in the difference between the magnitudes of the strained and unstrained reciprocal lattice vectors. [Recall that the mag-4 symmetric form factor makes no contribution, since

$\cos(\mathbf{g} \cdot \mathbf{s}) = 0$ .<sup>16</sup> For the reciprocal lattice vectors 10, 11, 13, and 14, the magnitude squared of the strained reciprocal lattice vectors is unchanged.

The symmetry-breaking effects of shear strain can be represented in the slight differences given in Eq. (A5). This difference leads to the splitting of the light- and heavy-hole bands, as well as band curvature changes. The additional fit parameter,  $D_4^A$ , is essentially the derivative of the antisymmetric form factor. We empirically fit this parameter to match the observed splitting, which is approximately equal to

$$\Delta E_{\text{lh}} - \Delta E_{\text{hh}} = 2S - 2S^2/\Delta,$$

$$S = (-b) \frac{C_{11} + 2C_{12}}{C_{11}} \varepsilon, \quad (\text{A6})$$

in which  $b$  is the shear deformation potential, and  $\Delta$  is the spin-orbit split-off energy.<sup>17</sup>

In addition, symmetry breaking also occurs in the form factors at mag-8, mag-11, and higher. We have empirically determined that these higher-order symmetry breaking effects are not needed in the empirical band fitting of the conduction- and valence-band energies and curvatures near zone center. The end result is that only seven pseudopotential form factors (the six described in Ref. 3 and the parameter  $D_4^A$ ), plus one spin-orbit fit parameter,  $\Gamma$ , are needed to fit the

bands of a strained zinc-blende material. The parameters for InAs under tensile strain on a GaSb substrate are shown in Table I.<sup>10</sup> The InAs was coherently strained to 0.62% tensile strain. The hydrostatic component of this strain reduced the InAs band gap by an amount 33.4 meV as given by Eq. (A4). The pseudopotential form factors in Table I reproduce this slight band-gap reduction. As explained earlier, the shear strain is included in the superlattice calculation by including the parameter,  $D_4^A$ , in the strained InAs fit. The value given in Table I splits the light- and heavy-hole bands by 47.8 meV, again in good agreement with Eq. (A6).

If we use this approach to represent the strained materials, provided that the strained material form factors give good agreement with the strained material band diagram, we can calculate the properties of strained layer superlattices by directly applying the lattice-matched methods. For a two-component superlattice containing coherently strained well material in an unstrained barrier, the approximate superlattice effective potential is given as a direct superposition of component material pseudopotentials as

$$V(\mathbf{r}) = \text{rect}\left(\frac{z}{w}\right) \sum_{\mathbf{g}} \Omega_{\mathbf{g}}^W e^{i\mathbf{g} \cdot \mathbf{r}} + \left[1 - \text{rect}\left(\frac{z}{w}\right)\right] \sum_{\mathbf{g}} V_{\mathbf{g}}^B e^{i\mathbf{g} \cdot \mathbf{r}}. \quad (\text{A7})$$

The remainder of the calculation proceeds as described for lattice-matched materials in Ref. 3.

<sup>1</sup>D. L. Smith and C. Mailhot, Rev. Mod. Phys. **62**, 173 (1990).

<sup>2</sup>D. M. Wood and A. Zunger, Phys. Rev. B **53**, 7949 (1995).

<sup>3</sup>G. C. Dente and M. L. Tilton, J. Appl. Phys. **86**, 1420 (1999).

<sup>4</sup>M. J. Shaw, Phys. Rev. B **61**, 5431 (2000).

<sup>5</sup>A. P. Ongstad *et al.*, J. Appl. Phys. **89**, 2185 (2001).

<sup>6</sup>R. Kaspi *et al.*, Appl. Phys. Lett. **76**, 409 (2000).

<sup>7</sup>R. Kaspi *et al.*, Appl. Phys. Lett. **79**, 302 (2001).

<sup>8</sup>L. Wang *et al.*, Phys. Rev. B **60**, 5590 (1999).

<sup>9</sup>G. A. Sai-Halasz, R. Tsu, and L. Esaki, Appl. Phys. Lett. **30**, 651 (1977).

<sup>10</sup>Landolt-Bornstein, *Numerical Data and Functional Relationships in Science and Technology* (Springer-Verlag, Berlin, 1987).

<sup>11</sup>A. Zunger (private communication).

<sup>12</sup>M. E. Flatte and W. H. Lau (private communication).

<sup>13</sup>R. Magri and A. Zunger, Phys. Rev. B **64**, 081305 (2001).

<sup>14</sup>R. Kaspi (private communication).

<sup>15</sup>W. H. Lau and M. E. Flatte, Appl. Phys. Lett. **80**, 1683 (2002).

<sup>16</sup>P. Y. Yu and M. Cordona, *Fundamentals of Semiconductors* (Springer, New York, 1996).

<sup>17</sup>L. A. Coldren and S. W. Corzine, *Diode Lasers and Photonic Integrated Circuits* (Wiley, New York, 1995), p. 527.

<sup>18</sup>L. L. Chang *et al.*, J. Vac. Sci. Technol. **19**, 589 (1981).

<sup>19</sup>G. A. Sai-Halasz *et al.*, Solid State Commun. **27**, 935 (1978).

<sup>20</sup>H. Mohseni *et al.*, Appl. Phys. Lett. **19**, 1403 (1997).

<sup>21</sup>F. Fuchs *et al.*, Inst. Phys. Conf. Ser. **144**, 219 (1995).

<sup>22</sup>A. Zunger (private communication).

<sup>23</sup>E. Corbin *et al.*, Semicond. Sci. Technol. **16**, 263 (2001).